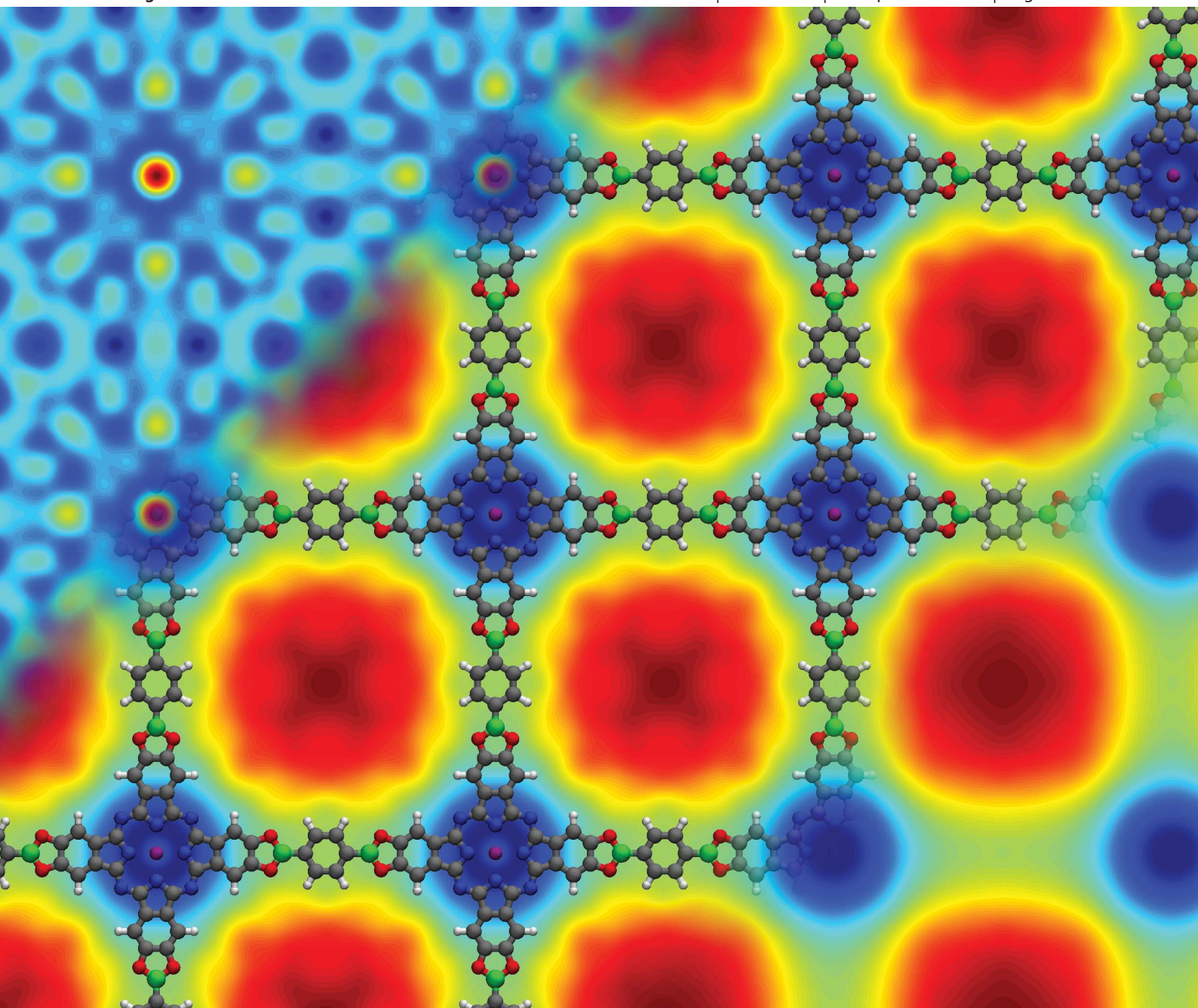


Journal of Materials Chemistry

www.rsc.org/materials

Volume 22 | Number 34 | 14 September 2012 | Pages 17351–18064



ISSN 0959-9428

RSC Publishing

PAPER

Paulette Clancy *et al.*

A classification scheme for the stacking of two-dimensional boronate ester-linked covalent organic frameworks



0959-9428 (2012) 22:34;1-C

A classification scheme for the stacking of two-dimensional boronate ester-linked covalent organic frameworks†

Brian T. Koo,^a William R. Dichtel^b and Paulette Clancy^{*a}

Received 30th March 2012, Accepted 20th June 2012

DOI: 10.1039/c2jm32009f

The interlayer stacking of thirty-three two-dimensional covalent organic frameworks (2D COFs) that derive from five boron-containing, “connectors” and seven hydrocarbon “linkers” was evaluated with a Molecular Mechanics (MM) approach, employing the MM3 potential of Allinger *et al.* Several of these COFs have been synthesized previously, whereas others are proposed structures. This comprehensive study allowed us to classify the nature of COF stacking in terms of potential energy surfaces (PES) and, further, to determine the origin of these surfaces in terms of combinations of repulsive electrostatic and attractive dispersion forces. None of these 2D COFs stack in the exact eclipsed configuration traditionally assigned to these materials; instead, adjacent layers adopt surprisingly similar small offsets (1.5–2.8 Å). For verification, PES of selected, important interlayer offsets were obtained using more accurate Density Functional Theory (DFT) calculations and shown to produce similar offsets to those derived from MM. The symmetry of the 2D COF networks allows the offsets to be accommodated in several degenerate directions, precluding the formation of interlayer stacking patterns with pervasive long-range order, such as staircase, helical, or zigzag arrangements. Although these offsets are often small relative to the size of the COF unit cell, they are sufficient to impede the filling of COF pores with large “guests”, such as fullerenes. Finally, we use a combination of topological, compositional, and interaction parameters to provide a simple correlation that allows researchers to predict inter-layer offsets and interaction energies without performing any molecular simulations. Uncovering such design principles should pave the way to target the creation of COFs with prescribed structures and charge transport properties.

Introduction

The initial discovery of covalent organic frameworks (COFs)¹ in 2005 has motivated the creation of many new COFs^{2–12} because of their predictable assembly, long-range order, high specific surface area, permanent porosity, and low density.^{1–3,6,8} COFs resemble zeolites and metal–organic frameworks, but are lower in density, spurring intense exploration of their potential in hydrogen storage,^{13,14} filtration,^{15,16} catalysis,¹⁷ and optoelectronics.^{4,8,10} With their customizable composition, COFs can include functional π -electron systems in their infrastructure such as pyrene and metallophthalocyanine units.¹⁸ They can also be grown as oriented thin films on conductive substrates,¹⁹ demonstrating a pathway to process these materials into devices.

These two- and three-dimensional structures are most commonly derived from condensation reactions of polyfunctional boronic acids and are comprised of organic subunits that we denote as either boron-containing “connectors” or hydrocarbon “linkers”. Each combination of connector and linker fragments forms specific topologies based on the geometry of reactive functional groups. The ability to create new COFs by varying these molecular building blocks means the class of COFs contains a staggering number of as-yet unsynthesized but potentially useful materials.

Since these applications of COFs rely heavily on structure, we propose a classification scheme and methodology to rapidly screen COFs for desired design criteria. Our methodology simplifies the task of designing new COFs by linking the energetics of stacking to the structure of individual COF fragments and proposes a new paradigm for the analysis of COFs. By comparing the potential energy surfaces (PES) of 2D COFs based on many different linkers and connectors, this paper will uncover generalizations of stacking behavior and propose correlations such that the structural properties of as-yet unsynthesized COFs with related chemical composition or topology may be predicted without simulation. We calculated the PES of 2D COFs constructed from one of five connectors: boroxine

^aSchool of Chemical and Biomolecular Engineering, Cornell University, Ithaca, NY 14853, USA. E-mail: Paulette.Clancy@cornell.edu

^bDepartment of Chemistry and Chemical Biology, Cornell University, Ithaca, NY 14853, USA

† Electronic supplementary information (ESI) available: Simulated powder X-ray patterns of COFs, preferred offset correlations, description of molecular fragments used in Gaussian simulations, and superimposed topologies on top of potential energy surfaces for each COF. See DOI: 10.1039/c2jm32009f

(BRX), hexahydroxybenzene (HHB), hexahydroxytriphenylene (HHTP), dodecahydroxycoronene (DHC), or nickel-phthalocyanine (Pc), as well as one of seven linkers: pyrene (Py), phenylene (Ph), biphenyl (BP), diphenylacetylene (DPA), diphenylbutadiyne (DPB), 1,3,5-benzene (B), or 1,3,5-triphenylbenzene (TPB), shown in Fig. 1, in order to investigate preferred and energetically favorable stacking configurations. This combination of connectors and linkers yields thirty-three distinct 2D COFs, many of which have not yet been reported (see Table S1†).

Recent computational studies of 2D COFs have found that adjacent layers stack with small lateral offsets of about 1.0–1.7 Å,^{20–22} that are considerably more energetically favorable than perfectly eclipsed structures due to repulsive coulomb interactions. After determining the extent of interlayer offsets from the PES of all 33 COF structures, we assess the impact of such offsets on the ability of the COF to incorporate C₆₀ (a fullerene) into its pores. C₆₀ is a prototypical n-type semiconducting molecule used in planar and bulk heterojunction designs. COFs might be used as a scaffold to direct fullerene molecules within the pores, potentially allowing both electron and holes to travel through separate regions of the composite material. In this way, the interface between the two regions could give rise to an ordered heterojunction that facilitates the separation of excitons into free charge carriers.^{4,8} We compare surface diffusion in stacks of ideal (perfectly eclipsed) *versus* non-ideal COFs to highlight the significance of small distortions to the crystal structure on the ability to fill the pores with C₆₀ and hence create p–n heterojunctions.

Computational methods

The preferred lateral offset and interlayer spacing of 2D COFs were evaluated using potential energy surfaces, which tabulate

the intermolecular energies of two layers in all possible stacked configurations. They allow us to evaluate metastable positions and assess their influence on several aspects of the COF structure, including slip defects, lateral stability, and interlayer binding energies. We have used this approach previously to probe the nature of C₆₀-pentacene interactions,^{23,24} and found that the PES effectively describes and predicts experimental structures. Here we compute the intermolecular energy between laterally shifted configurations of 2D COF layers using inexpensive MM calculations²⁵ and validate these results through the judicious use of more expensive DFT calculations.²⁶

Molecular Mechanics allows us to compute intermolecular interactions using parameterized potentials that model physically observed interactions. All MM calculations were performed using the LAMMPS software package.^{27,28} We modeled the van der Waals interactions with the Buckingham potential from the Molecular Mechanics 3 (MM3) force field of Allinger *et al.*, to which we assigned a 9 Å cut-off^{25,29} and modeled the electrostatic interactions with a coulomb potential with a 10 Å cut-off using CHelpG-generated partial charges.³⁰ The semi-empirical MM3 force field provides an accurate description of the van der Waals interactions between the hydrogen, boron, carbon, nitrogen, and oxygen atoms found in COFs. We showed previously that this force field produced comparable results to *ab initio* MP2-derived intermolecular energies and good agreement with experimental properties for hydrocarbon and aromatic compounds.²³ The CHelpG method³¹ was used to fit values for atomic charges to the quantum mechanically derived electrostatic potential of 2D COF layer fragments (see ESI†). The use of small molecular fragments permitted calculation of these charges from DFT using the 6-311G(d,p) basis set and B3LYP hybrid functional.³¹ An Ewald summation³² provided closure for the long-ranged Coulomb

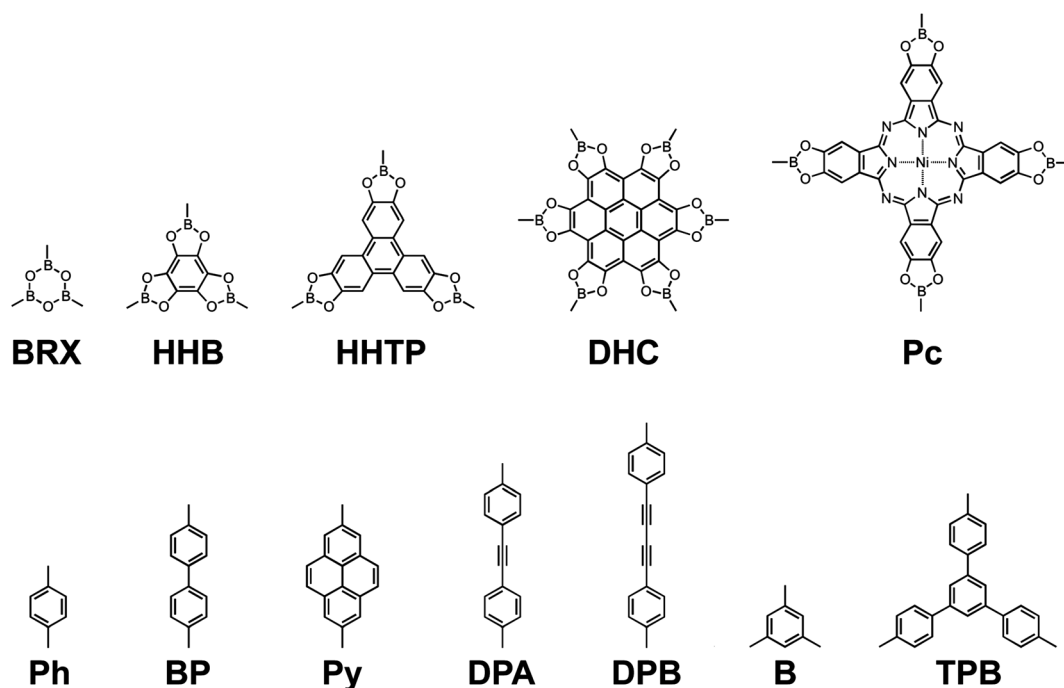


Fig. 1 Chemical structure of connector and linker components of the COFs in this study and their abbreviations. Top row connectors: boroxine (BRX), hexahydroxybenzene (HHB), hexahydroxytriphenylene (HHTP), dodecahydroxycoronene (DHC), nickel phthalocyanine (Pc). Bottom row linkers: phenylene (Ph), biphenyl (BP), pyrene (Py), diphenylacetylene (DPA), diphenylbutadiyne (DPB), 1,3,5-benzene (B), 1,3,5-triphenylbenzene (TPB).

potential beyond the 10 Å cut-off. Given the less expensive computational cost of the MM calculations, we modeled entire two-layer systems with slab-like periodicity, with each layer optimized individually in Gaussian 09 using the M06 functional and the 6-31G(d,p) basis set. Simulating two (nearest) layers is sufficient to capture the behavior of the system; the interaction between second nearest layers, which are separated by an average distance of 7 Å, contributes a 0.2 eV variation in potential energy over the entire unit cell, and only a 0.03 eV variation in potential energy if configurations with lateral offsets up to 3 Å are considered. Given the strong covalent bonds in each layer, we imposed a rigid sheet structure for the MM calculations.

Density Functional Theory representations of intermolecular interactions are invariably more accurate than corresponding MM interactions. With an appropriately chosen functional, DFT calculations can accurately describe π -orbital stacking, dispersion energies, and the electrostatic interaction energy between COF layers. Given the highly aromatic structures of the COF materials studied here, we chose the M06 functional developed by Zhao and Truhlar,²⁶ as implemented in Gaussian 09.³³ M06 is a meta-hybrid generalized gradient approximation functional parameterized for systems with non-covalent interactions and has been used in prior studies, by us and others,^{12,34–36} to model aromatic molecular systems with π -orbital stacking. Results using the M06 functional were undertaken to verify the MM-derived predictions of the PES. However, the computational cost of Gaussian only allows small fragments of representative COFs to be modeled. Thus, representative stacking motifs were chosen judiciously in conjunction with the MM simulations to focus on the most relevant regions of the PES. DFT was used to calculate the potential energy of two-layer configurations with lateral offsets up to 3 Å. For the DFT calculations, we modeled a motif that represented only a subset of each layer, where each subset consisted of a single connector unit fully terminated with hydrogen-capped linkers, as shown in Fig. S1.† The geometry of these motifs adopted the geometry of the optimized layer. Like in the MM calculations, we imposed a rigid structure for the DFT calculations.

The translational degrees of freedom in the system, described by an offset vector between layers, were explored by shifting one layer (MM calculations) or one motif (DFT calculations) relative to the other (layer/motif) in increments of 0.01 Å in the direction normal to the COF sheet (0.02 Å for DFT), and 0.1 Å in the directions parallel to the COF sheet. A higher resolution was used in the normal direction to reflect the narrow range of interlayer distances found in the literature for COFs. The component of the offset normal to the COF sheets was tested in the range 2.50–4.00 Å, which encompasses the experimentally determined layer spacing of 3.3–3.5 Å.^{1,8} The PES are thus represented by the configurations with the lowest energies along the normal.

Since appreciable interlayer offsets will inevitably reduce the pore void volume accessible to large guest molecules, our final study determined the effect of the offsets on a practical application, the viability of incorporating C₆₀, a prototypical n-type organic semiconductor of interest for photovoltaic devices, within the COF pores. Since surface diffusion is a prevalent mechanism of transport in mesoporous materials, we probed the potential energy of the pore surface of a representative COF,

here **HHTP-Ph (COF-5)**,¹ to determine the ease of surface diffusion. For this test, six stacked layers (a *z*-coordinate range of 20.4 Å) were fashioned into three configurations: helical, zigzag, and eclipsed, as shown in Fig. 2. The eclipsed configurations are stacked without offset; the helical and zigzag configurations are stacked by rotating the offset vector 60° and 180°, respectively, from layer to layer. The **COF-5** stacks were assumed to adopt an experimentally observed 3.4 Å interlayer spacing,¹ and the lateral offset of 1.6 Å was determined by MM data. The geometry of C₆₀ and **COF-5** were optimized with DFT using the M06 functional and 6-31G(d,p) basis set. Then a C₆₀ ad molecule was “rastered” across the pore surface, recording its MM-derived intermolecular energy at each location. The scanning was performed in cylindrical coordinates by translating the center of the C₆₀ probe between radial coordinates 0 and 13 Å in increments of 0.1 Å, and between azimuthal coordinates 0° and 360° in increments of 0.72° (500 sampled directions).

Results

A classification based on topology

We chose a classification scheme based on the underlying topology of the COF because each topology can be associated with a unique composition and unique pore shape. As shown in Fig. 3, each topology contains a different ratio of connectors to linkers. Topology **A** contains ternary connectors (**BRX**, **HHB**, and **HHTP**) and binary linkers (**Py**, **Ph**, **BP**, **DPA**, **DPB**) in a ratio of 2 : 3. Topology **B** contains ternary connectors and ternary linkers (**B**, and **TPB**) in a ratio of 1 : 1. Topology **C** is related to topology **B**, but with the entire second layer rotated 60° relative to the first layer. Topology **D** contains senary connectors (**DHC**) and binary linkers in a ratio of 1 : 3. Topology **E** contains the **DHC** connector and ternary linkers in a ratio of 1 : 2. Topology **F** contains quaternary connectors (**Pc** and **porphyrin**) and binary linkers in a ratio of 1 : 2.

The outlined region in Fig. 3 defines the two-dimensional unit cell for each of these topologies, and the solid black triangular region denotes the smallest representation of energies in the unit cell, which we call the primitive region. The fraction of the unit cell area covered by the primitive region reveals the symmetry of the potential energy surfaces. Hence in Fig. 3, topologies **A** and **B**

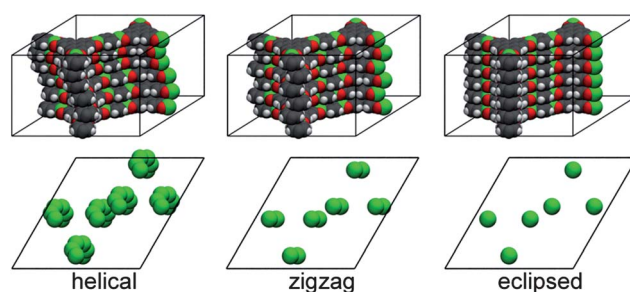


Fig. 2 Monoclinic unit cells each containing six **HHTP-Ph (COF-5)** layers stacked in helical, zigzag, and eclipsed patterns. The helical pattern is formed by rotating the offset vector 60° between layers. The zigzag pattern is formed by rotating the offset vector 180° between layers. The eclipsed pattern is a control structure testing the effect of no offset. The bottom set of images are overhead representations of unit cells showing boron atoms only.

have 6-fold symmetry, **C** has 3-fold symmetry, **D** and **E** have 6-fold symmetry, and **F** has 4-fold symmetry. COFs produced by a combination of ternary connectors and ternary linkers possess two distinct topologies, shown as topologies **B** and **C** in Fig. 3, that are not interchangeable by layer translation alone. We will focus below on studying two-layer motifs found near the vertices of the primitive region because each motif, as shown in Fig. 3 and 4, corresponds to layer configurations with dissimilar degrees of interaction between connector and linker fragments. Using this concept of the motif to explore a range of hypothetical stacking scenarios, we will link variations in the potential energy to specific structural features.

Assignment of regions on the potential energy surfaces

We assign all double layer configurations near the primitive region vertex at the center of each unit cell to region **1**. In this region, layer configurations are arranged such that every molecular fragment in one layer overlaps its molecular counterpart in an adjacent layer, as shown in the left diagrams in Fig. 4. Due to the heterogeneous nature of topology **C**, eclipsed configurations are not possible, so we assign to region **1** all configurations where connector fragments overlap linker fragments in adjacent layers, and linker fragments overlap connector fragments in adjacent layers. In general, region **1** consists of double layer configurations with the largest possible overlap between molecular fragments.

Of the two remaining primitive region vertices in Fig. 3, we define region **2** as the one that lies on a connector or linker fragment. As depicted by the center diagrams in Fig. 4, region **2** generally represents configurations in which interactions between linker fragments in adjacent layers are minimized. However, there are subtle differences in region **2** in each topology that originate from topological differences. In topology **A**, not all

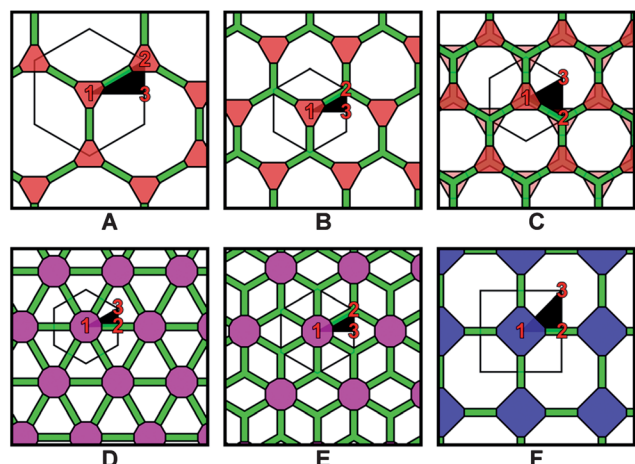


Fig. 3 COFs in this study can adopt one of six possible topologies shown here. Within each topology is the unit cell outlined in black, and the primitive region shown in solid black. Regions **1**, **2**, and **3** on the unit cell are denoted in red. (A) Ternary connector and binary linker. (B) Ternary connector and ternary linker. (C) Ternary connector and ternary linker (with top layer rotated by 60°). (D) DHC connector and binary linker. (E) DHC connector and ternary linker. (F) Pc connector and binary linker.

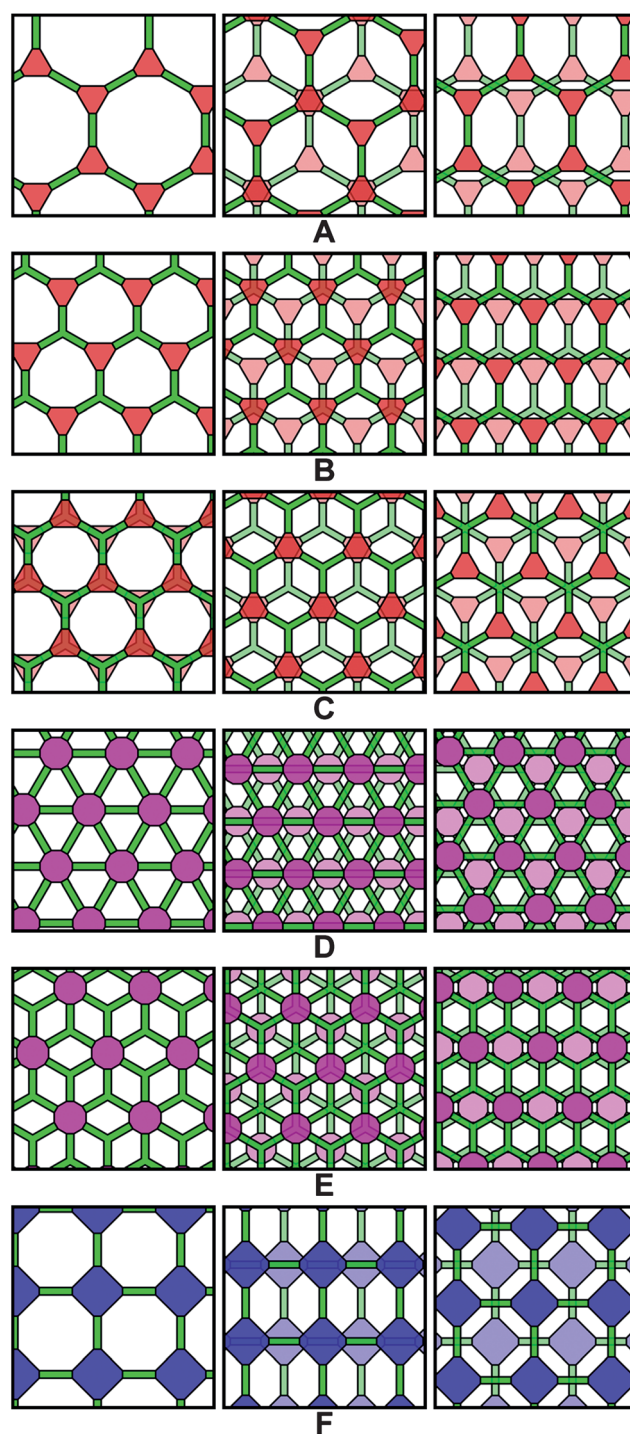


Fig. 4 Region **1** (left), region **2** (center) and region **3** (right) two-layer motifs from each of the six topologies described in Fig. 4. The two layers are differentiated by their shading.

connector fragments lie over molecular fragments in adjacent layers. Only half of the connectors have nearest neighbors and these nearest neighbors are stacked with a relative 60° rotational offset. In topology **B**, the interlayer interactions are not symmetric. Thus either all connector fragments have nearest neighbors in adjacent layers or all linker fragments have nearest neighbors in adjacent layers, but not both of these possibilities.

In topology **C**, the only interlayer interactions are between connector fragments, but in contrast to topology **A**, every connector fragment has a nearest neighbor. Similarly to topology **A**, every connector fragment interacts with a neighboring connector fragment in an adjacent layer *via* a 60° rotational offset. In topologies **D** and **E**, every molecular fragment has a nearest neighbor in an adjacent layer. In topology **F**, every connector fragment has a nearest neighbor that is a linker fragment. Given the 2 : 1 ratio between connector and linker fragments, half of the linker fragments do not have nearest neighbors.

The last primitive region vertex in Fig. 3 corresponds to region **3**, which generally corresponds to configurations with maximized linker–linker interactions. In all the topologies, the interactions are largely between linkers of one layer and linkers of an adjacent layer, and negligible interactions between connector fragments in adjacent layers. However, there are minor differences in region **3** in each of the topologies. In topologies **A**, **B**, **C**, and **D**, linker fragments interact with neighboring linker fragments *via* a rotational offset of 60° . In topology **E**, the linker–linker interaction consists of partially overlapped fragments, and in topology **F**, the linker–linker rotational offset is 90° . At the heart of this analysis is a combinatorial study of interactions between connector and linker fragments, and the weight of each interaction (connector–connector, connector–linker, and linker–linker) is governed by the underlying topology, as shown in Fig. 4.

Features of the potential energy surfaces

Fig. 5 shows a compilation of the molecular mechanics-derived PES of the COFs in this study. We arranged each PES in the figure according to its constituent building blocks (connector and linker molecular fragments), where the rows determine the connector, and the columns determine the linker. We normalized the potential energy with respect to the atom count per unit cell to collapse the potential energies onto the same range, and rescaled each plot according to its area. The rows, from top to bottom, correspond to **BRX**, **HBB**, **HHTP**, **DHC**, and **Pc** connectors. The columns, from left to right, correspond to **B**, **TPB**, **Py**, **Ph**, **BP**, **DPA**, and **DPB** linkers. In this compilation, the first three rows feature the PES of topologies **A**, **B**, and **C**. The PES in the last 5 columns are of topology **A**, the PES in columns one and three are of topology **B**, and the PES in columns two and four are of topology **C**. The fourth row features the PES of topologies **D** and **E**, where the first and third column are of topology **E**, and the last five columns are of topology **D**. The fifth row features the PES of topology **F**.

COFs with the same topology have the same types of interactions between connector and linker fragments in each region of the PES. Given the mostly hydrocarbon composition of connectors and linkers in this study, changes to the topography are due to changes in shape, length, and size of the connector and linker fragments. In most PES, these effects are subtle after normalization of the PES by the number of atoms per unit cell.

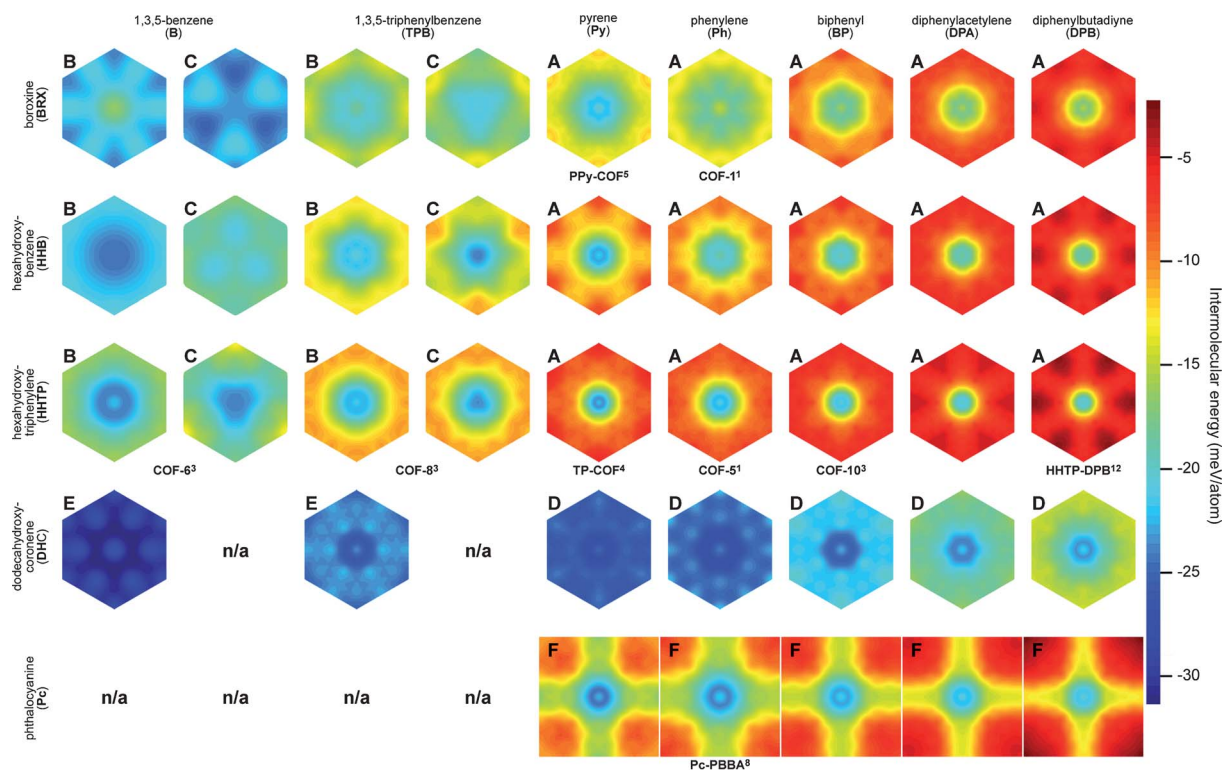


Fig. 5 Compilation of the 39 PES produced from the 33 COFs in the study. The topology is shown in the upper left hand corner of each PES. COFs that are labeled have been reported in literature, all others are proposed structures. The first three rows comprise COFs representing the **BRX**, **HBB**, and **HHTP** connectors, the fourth row comprises COFs representing the **DHC** connector, and the fifth row comprises COFs representing the **Pc** connector. The first four columns represent COFs with ternary linkers, and the last five columns represent COFs with binary linkers.

However, as a whole, COFs generally prefer to stack in region 1, with the intensity of this preference given by the depth of the potential energy well shown in Table S2.† An exception is **BRX-B**, which prefers to stack in region 2 when adopting topology **B**. In the topology **C** variant of stacking, **BRX-B** still prefers a much more staggered configuration. In topologies **A** and **F**, the PES contain a deep potential energy well at the center of the unit cell, in contrast to topologies **D** and **E**, which are flatter and more corrugated.

Dispersion and electrostatic interaction energies

To understand the origin of the features in the PES derived from molecular mechanics, we examined the dispersion and electrostatic components of the potential energy. The range of dispersion energies and electrostatic interaction energies (Table S3.1–3.3†) of stacked configurations governs the topography of the potential energy surface because the map of electrostatic interaction energy is highly corrugated, while the map of dispersion energy is relatively smooth. An example is the difference between COFs with topology **D/E** and COFs with topology **F**, as shown in Fig. 6. The range of dispersion energies of **DHC-Ph** is 3 meV per atom, whereas the range of dispersion energies of **Pc-Ph** is 17 meV per atom. Since the electrostatic interaction energies vary by similar amounts in both COFs, **Pc-Ph** resembles its dispersion energy surface, while **DHC-Ph** resembles its electrostatic interaction energy surface more closely. Since the dispersion energy ranges vary more broadly than the electrostatic interaction energy ranges, we attribute stabilizing effects mostly to the dispersion energy. At a low dispersion energy range (for example **BRX-B**, 2 meV per atom), the highly corrugated electrostatic interaction surface dominates the overall potential energy, producing a PES that is similarly corrugated. At a high dispersion energy range (for example **HHTP-DPB**, 18 meV per atom), the PES mostly adopts the features of the dispersion energy surface, effectively tuning out the corrugations of the electrostatic interaction surface.

The magnitude of the dispersion energy range originates from the projection of the atomic overlap between two stacked COF sheets. The projected atomic overlap is high at the center of the

PES, which produces large dispersion energies. In contrast, the projected atomic overlap is considerably reduced at the perimeter of the PES, which produces small dispersion energies. Consequently, COFs with larger pores such as those of topology **A** or **F** can reduce their overlap significantly by adopting configurations at the perimeter of the PES, while COFs with smaller pores (topologies **D** and **E**) cannot. Linker lengths relate directly to the size of the pore, so the dispersion energy range and also the lateral stability of stacked layers increases with increasing linker length.

The preferred offset that results in the lowest potential energy is generally not found at the exact center of the PES but at a slightly offset position. Because each COF atom possesses a partial atomic charge, the most favored configuration minimizes the repulsive interaction between charges of the same sign. Both electrostatic interaction surfaces in Fig. 6 are repulsive at their center, thus perfectly eclipsed configurations are unfavorable. However, as shown by the dispersion energy surfaces, eclipsed configurations are favorable. A balance between maximizing dispersion and minimizing electrostatic repulsions produces a set of preferred offsets that encircle the center of the PES. An exception to this general rule is **BRX-B**, which prefers a staggered configuration, and all COFs adopting topology **C**, which prefer to stack perfectly eclipsed with discrepancies at the smaller pore sizes. The stabilizing and destabilizing effects of the dispersion and electrostatic interaction energy in region 1 are generally coupled, but in the case of topology **C**, the electrostatic repulsion between layers is negligible because of the heterogeneous nature of the layers. Stacking in the configuration of Fig. 3C maximizes the dispersion energy and minimizes the electrostatic interaction energy, yielding a single lowest energy configuration, as seen in **HHB-TPB**, **HHTP-B**, and **HHTP-TPB**.

Besides the potential energy well at the center of the PES, the existence of other potential energy wells can be explained by analyzing the dispersion and electrostatic interaction energies. The PES of **BRX-Py** and **BRX-Ph** contain local minima in region 2 because of stabilizing electrostatic interaction energies. As mentioned above, region 2 configurations of topology **A** stack such that connector fragments overlap with a 60° rotational offset, as shown in Fig. 4A. The rotational offset ensures that highly electronegative atoms (oxygen) do not remain in the proximity of highly electropositive atoms (boron). This effect is more strongly seen in **BRX** than in **HHB** or **HHTP** COFs because boroxine contains more strongly partially charged boron and oxygen atoms. For COFs adopting topology **C**, the 1,3,5-benzene linker COFs contain local minima in region 3, while the **TPB** linker COFs contain local minima in region 2. This is because every carbon bonded to boron in the 1,3,5-benzene linker is more electronegative than the carbon atoms in the central aromatic ring of the **TPB** linker. Therefore, stacking in region 3 is more stabilized in 1,3,5-benzene COFs than in **TPB** COFs. There are local minima in region 3 of the PES of **Pc-Py** due to the stabilizing effects of the predominantly linker–linker interactions. The pyrene linker, which is bulky at the center but narrow at the ends, promotes a stacking configuration in which the centers of the linkers are overlapped to maximize the local dispersion energy. The existence of local minima on the PES can drastically affect the pore structure and

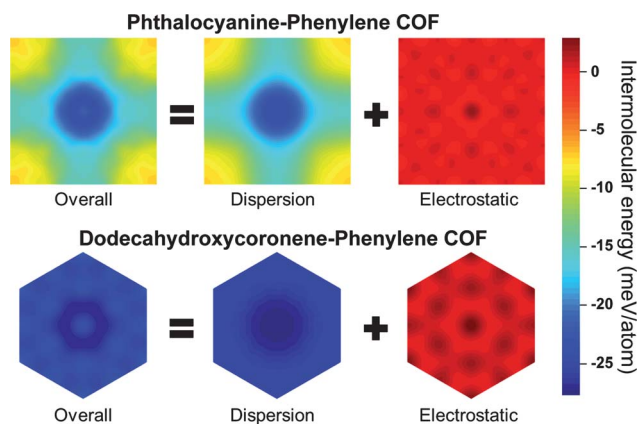


Fig. 6 Representation of the total potential energy surfaces of **Pc-Ph** and **DHC-Ph** separated by dispersion and electrostatic interaction energy components.

pore volume by inducing crystalline faults when these COF layers stack.

The methodology of analyzing individual component–component interactions shown here can be applied to COFs with new types of linkers and connectors if they possess the same topology. Although we have only studied hydrocarbon linkers, it is possible that COFs incorporating functionalized or polar linkers may produce distinctly different PES. However, understanding the behavior of other hydrocarbon linkers combined with known connectors may be facilitated by comparing potential energy surfaces in a manner similar to those in this study.

Verification by Density Functional Theory

It is important at this point to verify that the preceding results, obtained using semi-empirical MM models, were sufficiently accurate to be used in a predictive manner. Thus, we calculated the PES using DFT, in the manner described in the Methods section. As shown in Fig. 7, a number of new features are evident from a DFT-generated scan of region 1 of the PES of **HHTP-DPB**. There is a large 9 meV per atom (0.2 eV per formula unit) energy barrier at the center of the PES (1 meV per atom in MM calculations), which prevents layers from adopting a perfectly eclipsed configuration. COF layers cannot shift laterally over this barrier because the energy is orders of magnitude larger than thermal energies at room temperature. When “sandwiched” between layers in the bulk structure, COF layers are effectively fixed in non-eclipsed positions. The lateral offset that minimizes the potential energy is approximately 1.7 Å (compared with an 1.6 Å offset predicted by MM), and is independent of direction from the center. The variation of the potential energy at this offset is essentially insignificant, implying that all configurations with an offset of 1.7 Å are equally accessible at room temperature. One outcome of this result is that the COF layers are likely to stack in random patterns with no predictable stacking pattern.

The PES given by the **HHTP-DPB** COF possesses rotational symmetry of the offset vector, allowing us to condense the PES scan to a single scan direction without loss of generality. Given the rather similar chemical composition of the entire class of COFs, we have extended this assumption to eight COFs. From these one-dimensional scans, we determined the lateral offset at

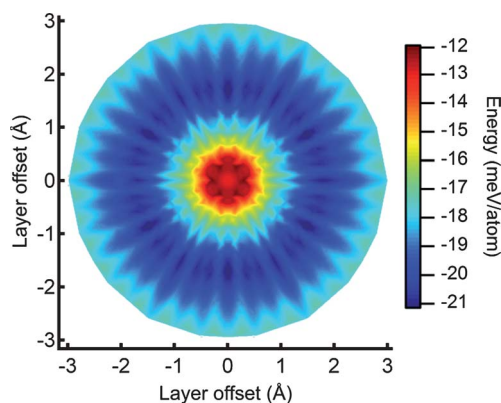


Fig. 7 Plot of the potential energy of region 1 of **HHTP-DPB** calculated by Density Functional Theory. The preferred lateral offset shown here is 1.7 Å.

which the intermolecular energy was minimized. Table S4† shows a comparison of the preferred lateral offsets generated using DFT to those obtained from MM, which were sampled from COFs representing four of the five connectors. Two results are immediately obvious: the lateral offset of six out of eight COFs have very similar offsets, and the offset computed by DFT and MM methods are in good agreement. The two methods differ insignificantly by 0.2 Å, with the exception of **DHC-Ph**, which differs by 0.7 Å. This large discrepancy may arise from the extended aromatic system of **DHC**, which cannot be accurately described by point charges. The qualitative agreement of features is such that we can be confident that energies derived from MM are sufficiently accurate.

Correlations of lateral offsets and predictive capability for new COFs

Our MM-generated results predict that the preferred lateral offset of non-rotated stacked COF layers varies from 1.5 to 2.8 Å across the range of thirty-three 2D COFs studied. We used a least squares regression to extract information related to this variation in offset. Ultimately, our intention in measuring the preferred offset vector was to use our numerical results to correlate this offset against easily measured physico-chemical properties. This would allow researchers designing potential COF structures to predict important structural features, such as preferred offsets, without having to undertake any molecular simulations. With

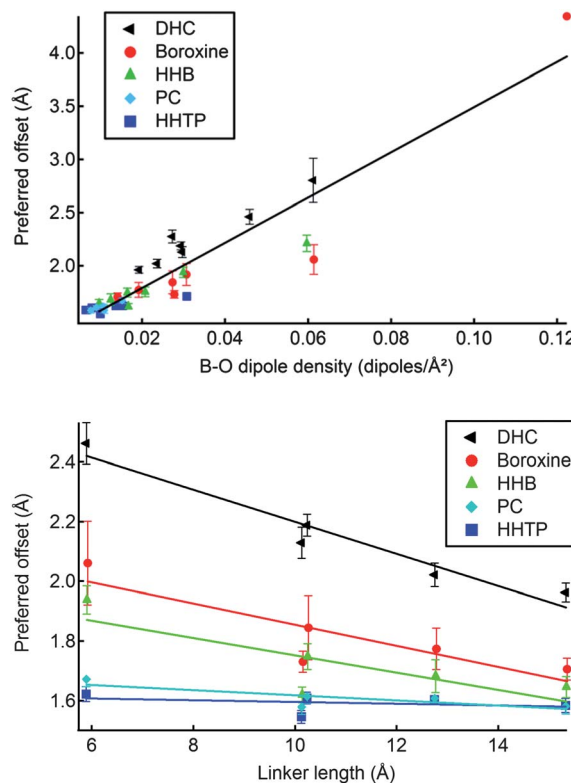


Fig. 8 Top: preferred lateral offset plotted against the area density of boron and oxygen dipoles. Bottom: preferred lateral offset plotted against linker length (binary linkers only). Regression lines are added to guide the eye.

this goal in mind, we looked at four correlations for the preferred offset, with respect to boron–oxygen dipole density, boron–oxygen density, atomic density, and linker length, with varied success. Even the less successful correlations may provide insight to experimentalists, and their details are given in the ESI.†

Given the pervasive presence of boron and oxygen atoms in the COFs studied here and the strong electrostatic forces between them, it seemed prudent to correlate the preferred offset with the boron–oxygen dipole area density. This density was calculated by normalizing the boron and oxygen dipole counts with the unit cell area. As shown in Fig. 8, this produced an r^2 value of 0.87, the strongest correlation that we obtained. This finding is intuitive since boron and oxygen are strongly electropositive and electronegative, respectively, and thus can be expected to repel strongly if placed in an eclipsed layer configuration. A larger percentage of boron and oxygen in the COF layer leads to more opposition to an eclipsed stacking and a larger lateral offset.

So far, the correlations have focused on relationships based on the nature of the connector. But exploring the prediction of offset in terms of linker length is also interesting, since it directly affects the pore size. As shown in Fig. 8, for any given connector, a linear correlation between offset and linker length is evident, but

each linear correlation differs in slope. The difference in offset between members of a given connector is small, no more than 0.4 Å. As shown in Fig. 8, offsets for COFs with **Pc** and **HHTP** connectors are essentially independent of linker length. Offsets of COFs with **HHB**, **BRX**, and **DHC** connectors showed slightly stronger dependence on the linker length, suggesting that pore topology (**DHC**) and high density of electropositive and electronegative atoms (**BRX** and **HHB**) may play some role.

Pore structure and accessible volume

The accessibility of many equivalent offset orientations in the results above implies that the pore structures of COFs are far more disordered (on the length scale of the layer-to-layer distance) than can be measured by X-ray diffraction studies. Based on our results, we hypothesize that 2D COF structures exhibit highly corrugated pore surfaces created by the shifted layers. To test the effect of a disordered pore structure on the incorporation of large spherical molecules, we probed the interaction between C_{60} and the inner surfaces of a representative COF (**COF-5**) in helical, zigzag, and eclipsed stacking patterns, chosen as representative cases. For this COF, the PES is

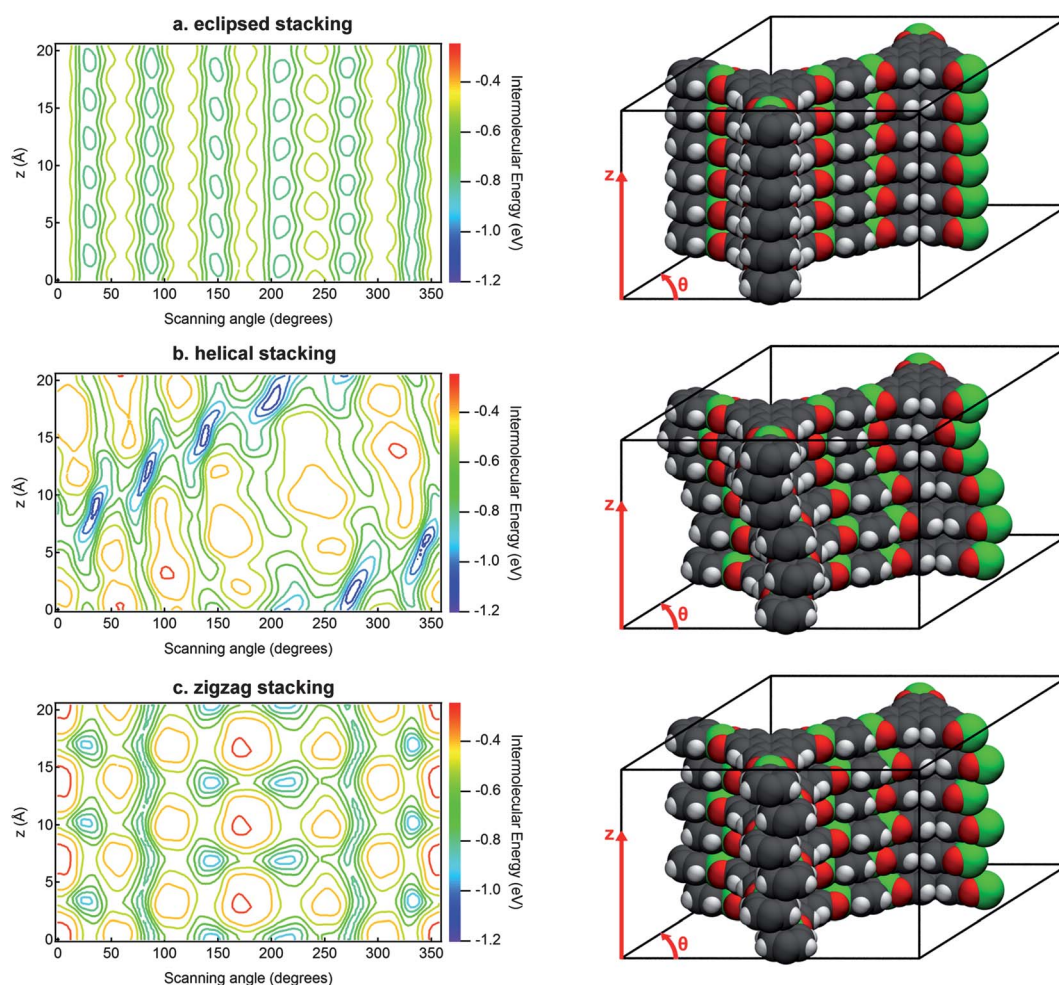


Fig. 9 PES of the inner surfaces of representative **HHTP-Ph (COF-5)** stacking structures as scanned by a C_{60} probe. The scanning angle is labeled as θ on the model structures. (a) Eclipsed stacking refers to layers that are stacked without an offset. (b) Helical stacking refers to layers that are stacked with the offset vector rotated 60° from layer to layer. (c) Zigzag stacking refers to layers that are stacked with the offset vector rotated 180° from layer to layer.

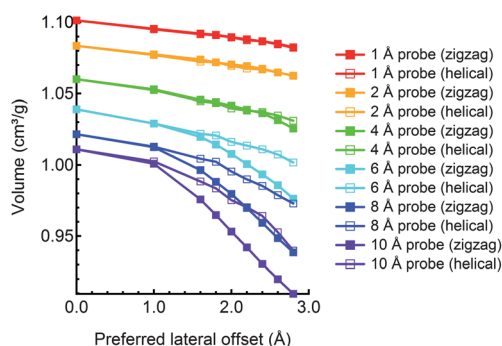


Fig. 10 Accessible pore volume of HHTP-Ph (COF-5) calculated with lateral offsets ranging from 0.0–2.8 Å and spherical probe sizes between 1 and 10 Å in diameter. The representative helical and zigzag stacking modes were also included.

anisotropic and highly corrugated with a potential energy range of 1 eV. The topography of the potential energy surface shows the existence of six low-energy pathways aligned with the *z*-axis, which correspond to the corners of the COF pore.

Viable transport of C_{60} within the pore requires the surface diffusion barriers to be small. As shown in Fig. 9, the eclipsed stacking pattern presents the most favorable PES for C_{60} diffusion, since it consists of six chains of connected potential energy wells with barriers of 0.1 eV. However, our studies of the preferred offset clearly show that the eclipsed structure is unlikely to form. In contrast, the surface diffusion barriers of the helical and zigzag stacking patterns are significant. In the helical structure, the potential energy wells are isolated along the low energy pathways, requiring fullerene molecules to diffuse through the COF pore while crossing over energy barriers of around 0.5 eV. In the zigzag stacking pattern, there are both isolated potential energy wells and connected potential energy wells. Transport is efficient along the connected potential energy wells located at scanning angles 90° and 270° . The net result is that randomly stacked COF layers will inevitably lead to trapping of fullerene molecules at positions inside the pore where the COF layers transition among the stacking patterns. Because of the set of preferred offsets observed here, no long-range orientationally ordered pore structures exist, except in simulations of a few stacked layers. Thus, the use of helical and zigzag structures are more accurate for describing the types of barriers likely to be encountered by fullerene molecules than prescribing the types of stacking modes found in bulk materials, and both these patterns show that energy barriers will significantly impede fullerene inclusion into the pores.

As the preferred lateral offset increases, it reduces the volume of the pore accessible to guest molecules. As shown in Fig. 10, the reduction in volume for a 1 Å diameter spherical probe from an eclipsed structure to one with a 2.8 Å offset is almost negligible (about 1%). In contrast, the reduction in volume for a 10 Å diameter probe like C_{60} is 10%. Combined with the change in pore structure and the tendency of close-packed C_{60} to favor orthogonal pores, the packing density is considerably lower. For COFs with large offsets, the volume between zigzag and helical structures are similar. Not surprisingly, the volume of the COF is less sensitive to the preferred lateral offset and stacking mode if a small probe is used. Therefore, for applications involving small

guest molecules, like hydrogen storage, the layer offsets do not modify the storage capacity appreciably.

Conclusions

We have performed a comprehensive study of the set of 2D COFs derived from five connectors and seven known linkers, covering a diverse range of lengths, compositions, and topologies. This study provides a basis for predicting COF stacking characteristics, which will be invaluable as the trend continues in constructing COFs with larger and more varied pores; it also provides a basis for exploring COFs composed of the optoelectronically significant phthalocyanine connector. Despite their variety, we found that the preferred offset for each of the 33 COFs we studied was surprisingly similar. Although we have shown that COFs with larger pores may resist lateral shifting more strongly and possess more lateral stability, they are less rigid. Consequently, the rigid layer assumption used in this study may be less accurate in predicting the stacking behavior of the larger pore COFs. We also provided a simple correlation of the predicted offset in terms of the boron–oxygen dipole density, which will allow researchers to predict offsets and inter-layer interaction energies without performing any simulations. From the correlations we provide for the preferred lateral offset, the offset can be moderately controlled by adjusting the boron–oxygen dipole density or the linker length, both of which have strong correlation values. Finally, although small, the predicted offsets of 1–2 Å are sufficient to impede the filling of COF pores with large guest molecules. Results for other COFs are likely to produce the same, if not higher, surface diffusion barriers because their offsets are greater or equal to the one tested here. Surface modification may be necessary to incorporate large spherical molecules in COFs. In addition, it is likely that hole transport through the stacks may be affected by this lateral shifting on the order of angstroms.³⁷ With this method and our COF classification scheme, we have shown that it is possible to rapidly explore the PES of candidate COFs with new connectors and new types of linkers and suggest design principles to target the creation of COFs with desired properties.

Acknowledgements

BTK would like to acknowledge the financial support of an NSF IGERT award: A Graduate Traineeship in Materials for a Sustainable Future, award no. 0654193. WRD acknowledges support by a NSF CAREER award (CHE-1056657) and a 3M non-tenured Faculty Award.

References

- 1 A. P. Côté, A. I. Benin, N. W. Ockwig, M. O'Keeffe, A. J. Matzger and O. M. Yaghi, *Science*, 2005, **310**, 1166.
- 2 R. W. Tilford, W. R. Gemmill, H.-C. zur Loye and J. J. Lavigne, *Chem. Mater.*, 2006, **18**, 5296.
- 3 A. P. Côté, H. M. El-Kaderi, H. Furukawa, J. R. Hunt and O. M. Yaghi, *J. Am. Chem. Soc.*, 2007, **129**, 12914.
- 4 S. Wan, J. Guo, J. Kim, H. Ihée and D. Jiang, *Angew. Chem., Int. Ed.*, 2008, **47**, 8826.
- 5 S. Wan, J. Guo, J. Kim, H. Ihée and D. Jiang, *Angew. Chem., Int. Ed.*, 2009, **48**, 5439.
- 6 C. J. Doonan, D. J. Tranchemontagne, T. G. Glover, J. R. Hunt and O. M. Yaghi, *Nat. Chem.*, 2010, **2**, 235.

- 7 M. J. Bojdys, J. Jeromenok, A. Thomas and M. Antonietti, *Adv. Mater.*, 2010, **22**, 2202.
- 8 E. L. Spitler and W. R. Dichtel, *Nat. Chem.*, 2010, **2**, 672.
- 9 M. Dogru, A. Sonnauer, A. Gavryushin, P. Knochel and T. Bein, *Chem. Commun.*, 2011, **47**, 1707.
- 10 X. Feng, L. Chen, Y. Dong and D. Jiang, *Chem. Commun.*, 2011, **47**, 1979.
- 11 F. J. Uribe-Romo, C. J. Doonan, H. Furukawa, K. Oisaki and O. M. Yaghi, *J. Am. Chem. Soc.*, 2011, **133**, 11478.
- 12 E. L. Spitler, B. T. Koo, J. L. Novotney, J. W. Colson, F. J. Uribe-Romo, G. D. Gutierrez, P. Clancy and W. R. Dichtel, *J. Am. Chem. Soc.*, 2011, **133**, 19416.
- 13 S. S. Han, H. Furukawa, O. M. Yaghi and W. A. Goddard, *J. Am. Chem. Soc.*, 2008, **130**, 11580.
- 14 H. Furukawa and O. M. Yaghi, *J. Am. Chem. Soc.*, 2009, **131**, 8875.
- 15 R. W. Tilford, S. J. Mugavero, P. J. Pellechia and J. J. Lavigne, *Adv. Mater.*, 2008, **20**, 2741.
- 16 R. Babarao, S. Dai and D. Jiang, *Langmuir*, 2011, **27**, 3451.
- 17 S.-Y. Ding, J. Gao, Q. Wang, Y. Zhang, W.-G. Song, C.-Y. Su and W. Wang, *J. Am. Chem. Soc.*, 2011, **133**, 19816.
- 18 X. Ding, J. J. Guo, X. Feng, Y. Honsho, S. Seki, P. Maitarad, A. Saeki, S. Nagase and D. Jiang, *Angew. Chem., Int. Ed.*, 2011, **50**, 1289.
- 19 J. W. Colson, A. R. Woll, A. Mukherjee, M. P. Levendorf, E. L. Spitler, V. B. Shields, M. G. Spencer, J. Park and W. R. Dichtel, *Science*, 2011, **332**, 228.
- 20 B. Lukose, A. Kuc and T. Heine, *Chem.-Eur. J.*, 2011, **17**, 2388.
- 21 B. Lukose, A. Kuc, J. Frenzel, T. Heine and J. Beilstein, *Nanotechnology*, 2010, **1**, 60.
- 22 W. Zhou, H. Wu and T. Yildirim, *Chem. Phys. Lett.*, 2010, **499**, 103.
- 23 R. A. Cantrell and P. Clancy, *Surf. Sci.*, 2008, **602**, 3499.
- 24 R. A. Cantrell, C. James and P. Clancy, *Langmuir*, 2011, **27**, 9944.
- 25 N. L. Allinger, Y. H. Yuh and J.-H. Lii, *J. Am. Chem. Soc.*, 1989, **111**, 8551.
- 26 Y. Zhao and D. G. Truhlar, *Theor. Chem. Acc.*, 2007, **120**, 215.
- 27 S. Plimpton, *J. Comput. Phys.*, 1995, **117**, 1.
- 28 LAMMPS can be found at <http://lammps.sandia.gov>.
- 29 N. L. Allinger, X. Zhou and J. Bergsma, *J. Mol. Struct.*, 1994, **312**, 69.
- 30 C. M. Breneman and K. B. Wiberg, *J. Comput. Chem.*, 1990, **11**, 361.
- 31 C. Zheng and C. Zhong, *J. Phys. Chem. C*, 2010, **114**, 9945.
- 32 P. J. in't Veld, A. E. Ismail and G. S. Grest, *J. Chem. Phys.*, 2007, **127**, 144711.
- 33 M. J. Frisch, G. W. Trucks, H. B. Schlegel, G. E. Scuseria, M. A. Robb, J. R. Cheeseman, G. Scalmani, V. Barone, B. Mennucci, G. A. Petersson, H. Nakatsuji, M. Caricato, X. Li, H. P. Hratchian, A. F. Izmaylov, J. Bloino, G. Zheng, J. L. Sonnenberg, M. Hada, M. Ehara, K. Toyota, R. Fukuda, J. Hasegawa, M. Ishida, T. Nakajima, Y. Honda, O. Kitao, H. Nakai, T. Vreven, J. A. Montgomery, Jr, J. E. Peralta, F. Ogliaro, M. Bearpark, J. J. Heyd, E. Brothers, K. N. Kudin, V. N. Staroverov, R. Kobayashi, J. Normand, K. Raghavachari, A. Rendell, J. C. Burant, S. S. Iyengar, J. Tomasi, M. Cossi, N. Rega, J. M. Millam, M. Klene, J. E. Knox, J. B. Cross, V. Bakken, C. Adamo, J. Jaramillo, R. Gomperts, R. E. Stratmann, O. Yazyev, A. J. Austin, R. Cammi, C. Pomelli, J. W. Ochterski, R. L. Martin, K. Morokuma, V. G. Zakrzewski, G. A. Voth, P. Salvador, J. J. Dannenberg, S. Dapprich, A. D. Daniels, Ö. Farkas, J. B. Foresman, J. V. Ortiz, J. Cioslowski and D. J. Fox, *Gaussian 09, Revision A.1*, Gaussian, Inc., Wallingford CT, 2009.
- 34 N. Marom, A. Tkatchenko, M. Scheffler and L. Kronik, *J. Chem. Theory Comput.*, 2010, **6**, 81.
- 35 J. Vura-Weis, M. A. Ratner and M. R. Wasielewski, *J. Am. Chem. Soc.*, 2010, **132**, 1738.
- 36 A. P. Kaushik and P. Clancy, *Surf. Sci.*, 2011, **605**, 1185.
- 37 V. Coropceanu, J. Cornil, D. A. da Silva Filho, Y. Olivier, R. Silbey and J.-L. Brédas, *Chem. Rev.*, 2007, **107**, 926.